Chapter 6

Influence of Vegetation Cover on Regional Evapotranspiration in Semi-Arid Watersheds in Northwest China

Mir A. Matin and Charles P.-A. Bourque

Additional information is available at the end of the chapter

http://dx.doi.org/10.5772/52812

1. Introduction

Evapotranspiration (ET) is an important biospheric process whereby liquid water is vaporized from moist surfaces and from plant tissues [1]. It is one of the key processes in the hydrological cycle and the energy balance of watersheds. Level of ET from a surface is primarily dependent on the availability of moisture on the surface and the amount of energy available to evaporate that moisture. To understand and quantify ET, three conceptual definitions of ET exist in the scientific literature. Actual ET (AET) refers to the actual evaporation of liquid water from a surface under given atmospheric conditions. For the same atmospheric conditions, potential ET (PET) refers to the elevated evaporation of water when the amount of surface moisture is unlimited and vegetation conditions are ideal. Ideal conditions regarding vegetation is characterized by actively growing short vegetation covering a large surface area with unlimited supply of soil water [2, 3]. If the vegetation cover is standardized to grass or alfalfa, PET is considered as reference ET (i.e., ET_o) [1]. Understanding spatiotemporal trends in ET is critical to interpreting eco-hydrometeorological processes of complex landscapes [4]. Specific factors affecting ET are divided into three main categories, namely:

i. meteorological factors, including solar radiation, near-surface air temperature, wind velocity, and air humidity;

ii. surface factors, including surface water and soil water content; and

iii. plant factors, including rooting depth, leaf structure, and stomatal density and aperture [1, 5, 6].

Spatiotemporal variability in these factors determines the variability of ET across large areas. This variability increases as the complexity of the underlying terrain and vegetation cover intensifies.

Back and forth exchange of water vapor and liquid water from oases at the base of the Qilian Mountains (Northwest China) and from the Qilian Mountains to oases as surface and shallow subsurface flow has been previously shown to be a potentially significant mechanism in the long term maintenance of oases in westcentral Gansu, NW China [7]. In general, direct precipitation (rain + snow) to the foothills and oases at the base of the Qilian Mountains is inadequate to maintain vegetation in these areas. Maintenance of oases vegetation is shown to be dependent on the surface water flowing from the higher regions of the mountain range, where direct precipitation and snowmelt are greatest. Supply of atmospheric moisture that leads to the formation of precipitation in the mountains is sustained by seasonal ET at the base of the mountain range.

Influence of vegetation and landcover on local and regional climate is well documented in the scientific literature [7-9]. Changes in landcover result in changes in surface albedo, surface roughness, leaf area index (LAI), stomatal conductance, rooting depth, and soil texture and structure [10-12]. Changes in surface vegetation have been known to impact

i. the partitioning of net radiative energy into sensible and latent heat fluxes, and

ii. the formation of convective rainfall by affecting the state of the convective boundary layer [13].

Agricultural landuse affects climate by modifying the physiological attributes (e.g., canopy conductance) of the land [14].

2. AET-determination methods

2.1. Point measurements

Suitability of AET-measurement methods depend on the reasons for assessment and on the spatiotemporal dimensions of the problem. Measurement of AET is mainly done indirectly by measuring the effect of AET on the water and energy balance. *Rose and Sharma* [15] categorized AET-measurement methods into three broad categories, i.e.,

i. hydrological approaches, based on the residual of the water-budget equation;

ii. micrometeorological approaches, including the Bowen ratio [16], aerodynamic, and eddy covariance-based methods [17], and

iii. plant-physiological approaches at the scale of individual plants or groups of plants by collecting sap-flow or chamber measurements.

http://dx.doi.org/10.5772/52812

2.1.1. Hydrological methods

Hydrological methods include the soil-water balance and weighing-lysimeter methods [18]. AET-determination from the soil-water balance is possible with a rearrangement of the water-budget equation, such that

$$AET = P - R - D - \Delta S, \tag{1}$$

where P is the precipitation, R is the surface runoff, D is the soil drainage, and ΔS is the change in soil-water storage.

Each term in Eqn. (1) is given in unit catchment volume, in which proper delineation of catchment boundaries, distribution of precipitation and streamflow gauges, and accuracy of runoff are critical for the accurate assessment of AET [19].

Lysimeters are measuring devices with containers for soil and plants that estimate ET by measuring the difference in weight of water in individual containers [20]. Accuracy of AET with lysimeters rests on the precision of the weighing instrument and sampling frequency [18].

2.1.2. Micrometeorological methods

Micrometeorological methods estimate latent heat fluxes at potentially high temporal frequencies over homogeneous vegetation [18]. The Bowen ratio method estimates latent heat fluxes [i.e., λET (W m^{-2}), where λ is the latent heat of vaporization expressed in J kg^{-1}] from the ratio of surface energy to the Bowen ratio (non-dimensional), such that

$$\lambda ET = \frac{R_n - G}{1 + \beta}, \tag{2}$$

where R_n is the net surface radiation (W m^{-2}), G is the soil-heat flux (W m^{-2}), and β (Bowen ratio) is the ratio to sensible heat and latent heat fluxes estimated from air temperature and water vapor pressure gradients taken within the same sample of air [21], or

$$\beta = \gamma \frac{\Delta T_a}{\Delta e_a}, \tag{3}$$

where γ is the psychometric constant (0.67 hPa K^{-1}, at sea level) and ΔT_a (K) and Δe_a (hPa) are differences in air temperature and water vapor pressure taken at two separate levels [16].

The aerodynamic resistance method uses the atmospheric boundary-layer resistance to calculate the transfer of sensible heat (H; W m^{-2}) from the surface to the air [22] and is formally expressed as

$$H = \varsigma C_p \frac{T_s - T_a}{r_a}, \tag{4}$$

where r_a is the aerodynamic resistance (s m^{-1}), ς and C_p are the density and specific heat of the airmass involved (kg m^{-3} and J kg^{-1} K^{-1}, respectively), and T_s and T_a are the surface and air temperature (K). The aerodynamic resistance in Eqn. (4) is the most important and most difficult to define. Various methods have been proposed to estimate this resistance, many of which are summarized in [23]. Once H is determined, AET (i.e., AET = $\lambda ET \cdot \lambda^{-1}$) can be determined from

$$\lambda ET = R_n - G - H, \tag{5}$$

given corresponding measurements of R_n and G.

Eddy covariance facilitates determination of vertical fluxes of atmospheric gases (e.g., water vapor, carbon dioxide, and trace gases) and heat within the atmospheric boundary layer. Historical advancement of eddy-covariance concepts is summarized in [17]. Assuming that the vertical wind velocity is responsible for vertical fluxes of atmospheric gases and heat, there should be a high positive correlation between vertical wind velocities and individual fluxes [24]. The method monitors high-frequency fluctuations in vertical wind velocity (m s^{-1}) and water vapor mixing ratios (kg kg^{-1}), in estimating AET from the covariance of the two, i.e.,

$$\lambda ET = \lambda \overline{w'q'}, \tag{6}$$

where w' and q' are the instantaneous fluctuation (deviation from the interval mean) in vertical wind velocity and water vapor mixing ratio in a parcel of air.

The physiological approach determines AET for individual plants or groups of plants. Two of the more broadly used physiological methods, includes

1. the sap-flow method, and
2. the chamber method.

In the sap-flow method, sap flow in plants is assumed to be closely linked to plant transpiration and is quantified by applying heat pulses to the stem of plants and analyzing corresponding heat balances [18]. In a chamber setting, transpiring plants are enclosed in a transparent chamber and changes in within-chamber water vapor concentrations are quantified [25].

While AET-determination methods based on principles of micrometeorology and plant physiology provide suitable overall accuracy at point scales (within a few tens of metres), spatial interpolation of their results across entire landscapes is wholly inappropriate because of the inherent complexity of natural landscapes, particularly with respect to topography and landcover.

http://dx.doi.org/10.5772/52812

2.2. Regional estimates of AET from remote sensing-based data

For expansive landscapes, remote sensing (RS)-based methods have been gaining popularity during the past few decades with regard to estimating regional AET at daily, monthly, and annual time scales. Characterizing land-surface conditions with RS-based methods provides an important way of overcoming the difficulty of interpolating AET for complex landscapes [26]. Most methods using earth-observation data in approximating regional AET can be categorized into three main groups, i.e., methods based on:

i. the surface-energy balance equation [27-29];

ii. Penman-Monteith and Priestley-Taylor equations [30-32]; and

iii. the complementary relationship [33, 34].

While all methods require an assessment of available net energy at the surface (i.e., R_n-G) as primary input, they differ in the way they partition the energy into H and λET.

2.2.1. Surface energy balance

The surface-energy balance is based on the assumption that R_n is equal to the sum of H, λET, and G; the energy required for photosynthesis is insignificant here as it accounts for < 1% of incoming solar radiation [35]. Based on a rewriting of the surface-energy balance, the expression of latent heat flux becomes:

$$\lambda ET = R_n - G - H, \tag{7}$$

where

$$R_n = R_s \downarrow - R_s \uparrow + R_L \downarrow - R_L \uparrow . \tag{8}$$

In Eqn. (8), $R_s \downarrow$ and $R_s \uparrow$ represent incoming and outgoing shortwave radiation and $R_L \downarrow$ and $R_L \uparrow$, incoming and outgoing longwave radiation emitted by the atmosphere (including clouds, if present) and earth surface. Typically, R_n and G (generally expressed as a fraction of $R_s \downarrow$) are determined from sun-earth geometric relations and illumination angles imposed by variable terrain. Most of the functions and information for the determination of R_n and G are available in present day geographic information systems (GIS) and digital terrain models [36-39]. Reflected and emitted radiative components are estimated from surface albedo, land surface and air temperatures, and emissivities derived from RS-data, e.g., as those identified in Table 1.

Most popular among surface-energy balance models are the surface-energy balance system (SEBS; [29]) and surface-energy balance algorithm for land (SEBAL; [27]). A comprehensive review of various surface-energy balance procedures appearing in the scientitific literature can be found in [40]. The SEBS model uses Monin-Obukhov similarity theory for the atmos-

pheric surface layer to derive land surface physical parameters and roughness lengths in determining the evaporative fraction at the limiting ends of accessible water, i.e., dry and wet limits [29]. At the dry end, evaporation (ET_{dry}) is assumed to be zero due to the limitation in soil moisture and, as a result, sensible heat (H_{dry}) is maximum, equalling net available energy (i.e., $H_{dry} = R_n - G$). At the wet end, evaporation (ET_{wet}) is assumed to be at its potential rate (i.e. $\lambda ET_{wet} = \lambda PET$) and sensible heat ($H_{wet}$) is minimum. Relative evaporation fraction is defined as:

$$EF_r = 1 - \frac{H - H_{wet}}{H_{dry} - H_{wet}}, \tag{9}$$

where H is the actual sensible heat flux and determined by solving a system of non-linear equations proposed by *Brutsaert* [29, 41]. AET is subsequently calculated with:

$$AET = \frac{1}{\lambda} EF_r \times \lambda PET, \tag{10}$$

where

$$\lambda PET = R_n - G - H_{wet}. \tag{11}$$

H_{wet} is calculated using an equation proposed by *Meneti* [42] based on the Penman-Monteith combination equation [43].

The SEBAL model [27] was designed to estimate regional AET from RS-data consisting of surface temperature, surface reflectance, Normalized Difference Vegetation Index (NDVI), and their corresponding relations. The SEBAL model calculates H from a linear relationship between T_s and T_a derived from plotted distributions of wet and dry pixels.

2.2.2. Penman-Monteith equation

To estimate regional ET using MODIS (or Moderate Resolution Imaging Spectroradiometer) data, *Cleugh et al.* [44] proposed the use of the Penman-Monteith equation, i.e.,

$$\lambda ET = \frac{\Delta(R_n - G) + \varsigma C_p \dfrac{e_s - e_a}{r_a}}{\Delta + \gamma\left(1 + \dfrac{r_s}{r_a}\right)}, \tag{12}$$

where Δ is the slope of the saturation-vapor-pressure-to-temperature-curve, r_a and r_s are the aerodynamic (atmospheric) and surface resistances (s m^{-1}) to the transfer of surface water vapor to the atmosphere, e_s is saturation vapor pressure (hpa), and e_a is actual vapor pres-

http://dx.doi.org/10.5772/52812

sure (hPa). In their model, input to Eqn. (12) are based on MODIS-derived vegetation data and daily surface meteorological data. Surface conductance is estimated in the model as a function of MODIS LAI and NDVI.

The model was later modified by *Mu et al.* [5] by adding vapor pressure deficit (VPD) and minimum air temperature as two important factors influencing stomatal conductance. In this modification, EVI (enhanced vegetation index; [45]) was used in replacing NDVI in the calculation of surface-vegetation fraction. Also, treatment of soil-water evaporation was incorporated. The model was further modified by *Mu et al.* [46] to include calculation of daytime and nighttime ET, soil-heat flux, and canopy conductance for both dry and wet foliar conditions. This variant of the model along with climate-station data worldwide were used in the production of a global product of AET (i.e., MOD16; [46]) that was subsequently validated against flux data acquired from 46 AmeriFlux sites distributed throughout the Americas.

2.2.3. Complementary-based methods

Complementary-based methods were first introduced by *Bouchet* [33], considering that whenever a well-watered surface dries, the decrease in AET is coupled with a corresponding increase in PET and, as a result

$$AET + PET = 2E_w, \tag{13}$$

where E_w is defined as the value of potential evaporation, when AET and PET are equal for an unlimited moist surface [47].

The complementary relationship is based on the assumption that the energy required for evaporation is permanently available [48]. In such instance, drying of a wet surface would result in a reduction in AET and a corresponding reduction in energy consumption. The energy saved would lead to an increase in PET [49]. The complementary relationship was extended by *Granger* [34] for non-saturated surfaces and non-equal changes in AET and PET. He expressed these changes as

$$\frac{\partial AET}{\partial PET} = \frac{-\gamma}{\Delta}. \tag{14}$$

Granger [34] defined PET, AET, and E_w using a Dalton-type mass-transfer equation and introduced an alternative equation for the complementary relationship, i.e.,

$$AET + PET\frac{\gamma}{\Delta} = E_w\frac{\Delta + \gamma}{\Delta}. \tag{15}$$

For non-saturated surfaces, *Granger and Gray* [50] proposed a relative evaporation fraction with the notion that wind velocity (u) has an equal impact on AET and PET, i.e.,

$$EF_r = \frac{AET}{PET} = \frac{f(u)(e_a^s - e_a)}{f(u)(e_s^s - e_a)} = \frac{e_a^s - e_a}{e_s^s - e_a}, \tag{16}$$

where e_s^s and e_a^s are the saturated and actual water vapor pressure at the surface (hPa), e_a is the actual water vapor pressure of the air (hPa), and f(u) is a function of wind velocity.

Two of the most widely used models based on the complementary relationship are

i. the advection-aridity (AA) model of *Brutsaert and Stricker* [51] and

ii. the complementary relationship aerial evaporation (CRAE) model of *Morton* [52].

The AA-model combines

1. the Priestley-Taylor equation [32],

2. the Penman equation [30],

3. an empirical wind-velocity function for relative evaporation [31], and

4. the complementary relationship, giving rise to

$$\lambda AET = (2\alpha - 1)\frac{\Delta}{\Delta + \gamma}(R_n - G) - \frac{\gamma}{\Delta + \gamma}0.35\ (0.5 + 0.54u_2)(e_s - e_a), \tag{17}$$

where α is the Priestley-Taylor constant (i.e., 1.26) and u_2 is the wind velocity at 2-m above the ground or canopy surface (m s^{-1}).

The CRAE model estimates AET from PET and E_w, i.e.,

$$AET = 2E_w - PET. \tag{18}$$

PET is addressed by decomposing the Penman equation into its two main components: one component to address the energy balance at the surface and another, the transfer of water vapor from a moist surface, or

$$\lambda PET = R_n - f_P f_T (T_P - T_a), \tag{19}$$

and

http://dx.doi.org/10.5772/52812

$$\lambda PET = f_T(e_s^p - e_a), \tag{20}$$

where e_s^p is saturation vapor pressure at T_p and T_p is the equilibrium temperature. The equilibrium temperature is defined as the temperature at which the energy balance [Eqn. (19)] and mass transfer [Eqn. (20)] give the same result for PET, when solved numerically. Parameter f_T is a vapor-transfer coefficient considered constant for a specific pressure level and independent of wind velocity. Parameter f_P is a function of atmospheric pressure (Ψ; hPa) and T_p, such that

$$f_p = \gamma\Psi + 4\varepsilon_s\sigma(T_p + 273)^3 / f_T. \tag{21}$$

E_w is calculated with a regression equation,

$$\lambda_E = b_1 + b_2\left(1 + \frac{\gamma\Psi}{\Delta_{TP}}\right)^{-1} R_{nTP}, \tag{22}$$

where b_1 and b_2 are coefficients determined by regression, Δ_{TP} is the slope of the saturation-vapor-pressure-curve at T_p, and R_{nTP} is the net surface energy at T_p, ε_s is the surface emissivity (non-dimensional), and σ is the Stefan-Boltzmann constant (i.e., 5.67×10^{-8} W m^{-2} K^{-4}).

The two models were validated by *Hobbins et al* [53] using long term water-balance estimates from 120 watersheds distributed throughout the United States. Outcomes of this validation have revealed that the AA-model underestimated the annual AET by 10.6% of annual precipitation and the CRAE-model overestimated the same variable by 2.5% of annual precipitation. For highly arid watersheds, both models tended to overestimate AET. Validation of complementary-based models in other regions of the world, as well as comparing their results with direct observations of AET and PET strongly support the prevalence of the complementary relationship. *Ramirez et al* [54] found that complementary-based models tended to work well for temperate, humid regions of the world and less well for arid regions [55].

One important constraint of conventional complementary-based methods is the requirement of wind velocity in the calculation of relative evaporation, which is not always available or reliable. To overcome this limitation, *Venturini et al* [56] modified the relative evaporation fraction (EF_r) of Eqn. (16) by replacing the expression of water vapor pressure with the corresponding temperature used in calculating it. In the case of actual surface water vapor pressure, a hypothetical temperature is used. This hypothetical temperature (T_u) is defined as the temperature at which the surface becomes saturated without changing water vapor pressure; this is equivalent to the definition of dew point temperature for air (T_d; K). Using these temperatures, *Venturini et al.* [56] modified Eqn. (16) to the following:

$$EF_r = \frac{AET}{PET} = \frac{T_u - T_d}{T_s - T_d}. \tag{23}$$

The hypothetical temperature (T_u) is derived using the slope of the water vapor pressure curve at T_d (i.e., Δ_d) and T_s (Δ_s) and the relationship between water vapor pressures and corresponding temperatures, such that

$$T_u = \frac{e_s^s - e_a - \Delta_s T_s + \Delta_d T_d}{\Delta_d - \Delta_s}. \tag{24}$$

Combining Eqn.'s (15) and (23) and the Priestley-Taylor equation [32] with the definition of E_w, the equation of AET then becomes

$$\lambda AET = \alpha \frac{EF_r \Delta}{EF_r \Delta + \gamma}(R_n - G). \tag{25}$$

These changes render the method less error prone and simpler regarding its data requirements. The method is numerically robust, producing errors < 15% of daily AET-measurements for heterogeneous landscapes of the Southern Great Plains of the United States [56]. *Kalma et al.* [57] summarized results of validation studies of 30 RS-based AET methods, where it was found that *Venturini et al.*'s [56] method produced the highest accuracy among the methods using MODIS-derived data. In the current study (Section 5.2), we use the *Venturini et al.* [56] method to calculate regional AET for the extremely complex landscape of westcentral Gansu, NW China.

3. Data requirements and accessibility

Data requirements in the calculation of AET depend on the method or model used in the calculation procedure. In general, input data for all methods can be grouped into four main categories:

i. surface meteorological data, including near surface air temperature, wind velocity, and in-air water vapor pressure and humidity;

ii. radiative energy fluxes, including incoming shortwave ($R_s \downarrow$) and longwave radiation ($R_L \downarrow$) and their outgoing counterparts (i.e., $R_s \uparrow$ and $R_L \uparrow$);

iii. surface attributes, including temperature, emissivity, albedo, and soil water content; and

iv. vegetation attributes, including LAI, vegetation-cover density and extent, and stomatal density and aperture.

http://dx.doi.org/10.5772/52812

These data can be

i. acquired by direct measurement in the field,

ii. derived from other related variables by means of regression, or

iii. derived from RS optical reflectance or thermal emission data.

While optical and thermal RS has been providing spatially-distributed values for the assessment of landscape AET, it poses several important challenges. RS-images from LANDSAT, ASTER, and SPOT-systems have high spatial resolution, but are acquired infrequently (i.e., every 16 days for LANDSAT and ASTER-systems and every 26 days for SPOT). In contrast, high temporal-acquisitions with geostationary satellites provide coarse spatial resolutions that are largely inadequate for regional-estimate of AET.

The MODIS-instrument is crucial to the production of important global image-products for land- and ocean-surface monitoring [58]. MODIS-instruments were launched to space by NASA (National Aeronautics and Space Administration) as part of the earth-observing system (EOS). MODIS Terra and Aqua image-products are available since February 24, 2000 and June 24, 2002, respectively [59]. Raw image-products have a temporal-acquisition interval of one or two days, covering 36 spectral bands between 0.405 and 14.385 μm [59, 60]. Besides daily image scenes, several composite-products are also available at multiple-day intervals at different processing levels. Level-1 products provide the instrument data at full resolution for individual MODIS scenes, which can be exploited after converting to radiance values, surface reflectance, or brightness temperature. Level-2, 2G, and 3 images contain derived geo-biophysical parameters, while Level-4 images contain model-generated products. Level-2G and -3 image-products consist of aggregations of daily images to give 8 and 16-day cloud-free images. Table 1 lists a number of MODIS image-products valuable in estimating regional AET.

Variables	**MODIS image-products**	**Spatiotemporal Resolution**	
		m	**days**
Land surface temperature (T_s) Land surface emissivity (ε_s)	MODIS land surface temperature and emissivity data (**MOD11A2**)	1000	8
Normalized difference vegetation index (NDVI) Enhanced vegetation index (EVI)	MODIS vegetation indices (**MOD13Q1**)	250	16
Land surface albedo (A_s)	MODIS products combined with **BRDF**-albedo products	1000	16
Air temperature (T_a) Dew point temperature (T_d)	MODIS atmospheric profile data (**MOD07**)	5000	1

Table 1. Data needed in the calculation of regional AET and corresponding MODIS image-product sources and spatiotemporal resolutions.

3.1. Land surface temperature

MODIS land surface temperatures (T_s; MOD11A2) are estimated from MODIS thermal infrared (TIR) data collected in near-cloud-free conditions with the application of a split-window algorithm to avoid misidentification with cloud-top conditions [61]. The algorithm uses MODIS-emissivity bands 31 and 32 in the calculation of T_s [62]. Details of the calculation-procedure can be found in [63].

3.2. Vegetation indices

MODIS vegetation-products (MOD13Q1) provide two vegetation-indices (VI) both at 250-m and 16-day resolution [64]. NDVI is calculated as the normalized ratio of near infrared (NIR) and red bands. EVI (introduced earlier) was developed to improve the sensitivity of NDVI for high biomass regions [45]. NDVI and EVI are calculated from

$$NDVI = \frac{\rho_{NIR} - \rho_{red}}{\rho_{NIR} + \rho_{red}}, \tag{26}$$

and

$$EVI = B\frac{\rho_{NIR} - \rho_{red}}{\rho_{NIR} + C_1\rho_{red} - C_2\rho_{blue} + L}, \tag{27}$$

where ϱ's are wavelength-specific atmospherically-corrected or partially atmosphere-corrected (for Rayleigh and ozone absorption) surface reflectances; B is the gain factor; L is the canopy background adjustment which addresses nonlinear, differential NIR and red-radiant transfer through vegetative canopies; and C_1, C_2 are the coefficients of aerosol resistance, which uses the blue band to correct for aerosol influences on the red band.

Coefficients adopted in the EVI-algorithm are L=1, C_1=6, C_2 = 7.5, and G= 2.5 [45]. While NDVI shows some problems with dense forests [45], both vegetation indices provide similar accuracy when used for cropland delineation [65].

3.3. Land surface albedo

Land surface albedo is the fraction of shortwave radiation reflected in all directions and is a critical parameter in estimating surface net shortwave radiation [66]. MODIS-BRDF (bidirectional reflectance distribution function)-based albedo image-products combine atmospherically-corrected surface reflectance from multiple dates and sensors in creating 16-day, 1-km resolution images [67]. The MODIS product, MCD43B3, includes both black and white sky

http://dx.doi.org/10.5772/52812

albedo acquired with the Terra and Aqua satellites [68], covering all seven spectral bands and three broad bands [60].

3.4. Air and dew point temperature

Air and dew point temperatures provided by the MODIS-MOD07 product (at 5-km resolution) is currently the best possible estimate of the two variables derived from RS methods [69]. MOD07 atmospheric profile information includes temperature and atmospheric humidity at 20 different vertical pressure levels between 5 to 1000 hPa [70].

4. Study area description

The study area consists of the Shiyang and Hei River watersheds in westcentral Gansu, NW China (Fig. 1). The Shiyang River originates from the Qilian Mountains and flows northwestward before terminating in the Minqin-lake district [71]. The total basin area is approximately 49,500 km^2. Elevation in the Shiyang River basin varies from 1,284 to 5,161 m above mean sea level (AMSL), with an average elevation of 1,871 m AMSL. The Hei River watershed, with a land surface area of approximately 128,000 km^2, is the second largest inland river basin in NW China [72]. The Hei River watershed includes the Zhangye watershed, with a total land area of about 31,100 km^2. Elevation in the Zhangye watershed varies from 1,287 to 5,045 m AMSL, with an average elevation of 2,679 m AMSL (Fig. 1).

The natural landscape of the study area comprises of mountains, oases, and deserts, all interacting with each other [73]. The oases play an important role in the sustainability of the region's overall ecological and socio-economic integrity [74]. The area overlaps four distinct ecoregions [75]. The northern part, noted for its arid to semi-arid conditions, includes portion of the Badain Jaran and Tengger deserts and oases in the southwest portions of the Alashan Plateau. Liangzhou, at the south, and Minqin, at the north, are two important oases in the Shiyang River watershed [71]. Zhangye is the main oasis in the Zhangye watershed. Spring wheat is the main food crop grown in the oases, which is usually supported by irrigation [76]. In the deserts, salt-tolerant, xerophytic shrub species, i.e., saxaul (*Haloxylon ammodendron*) and *Reaumuria soongolica* [77] are common.

Locally-generated rainfall in the oases is normally insufficient (< 170 mm yr^{-1}) to support agriculture in the oases [7]. The main source of water to the oases is the runoff from the Qilian Mountains generated from snowmelt and in-mountain precipitation transported by the Shiyang and Hei River systems [78, 79]. Glacial meltwater contributes to about 3.8% and 8.3% of total runoff in the Shiyang and Hei Rivers, respectively [78]. The meltwater usually flows during the spring-summer period due to the warming of the mountain glaciers and previous snow-season's snow cover [74].

A primary source of water in the rivers during the summer is orographic precipitation [80] formed in the Qilian Mountains [81]. Annual precipitation in the watersheds is < 80 mm in the desert-portion of the watershed and > 800 mm in the Qilian Mountains, proper. Annual

PET in the deserts ranges between 2,000 to 2,600 mm and 700 to 1,200 mm in the mountains [82]. Most of the precipitation occurs during June-August. About 94% of the water delivered from the mountains is through surface runoff. Average annual runoff delivered by the Shiyang River is about 15.8 ×10^8 m^3 and about 37.7 × 10^8 m^3 by the Hei River [82].

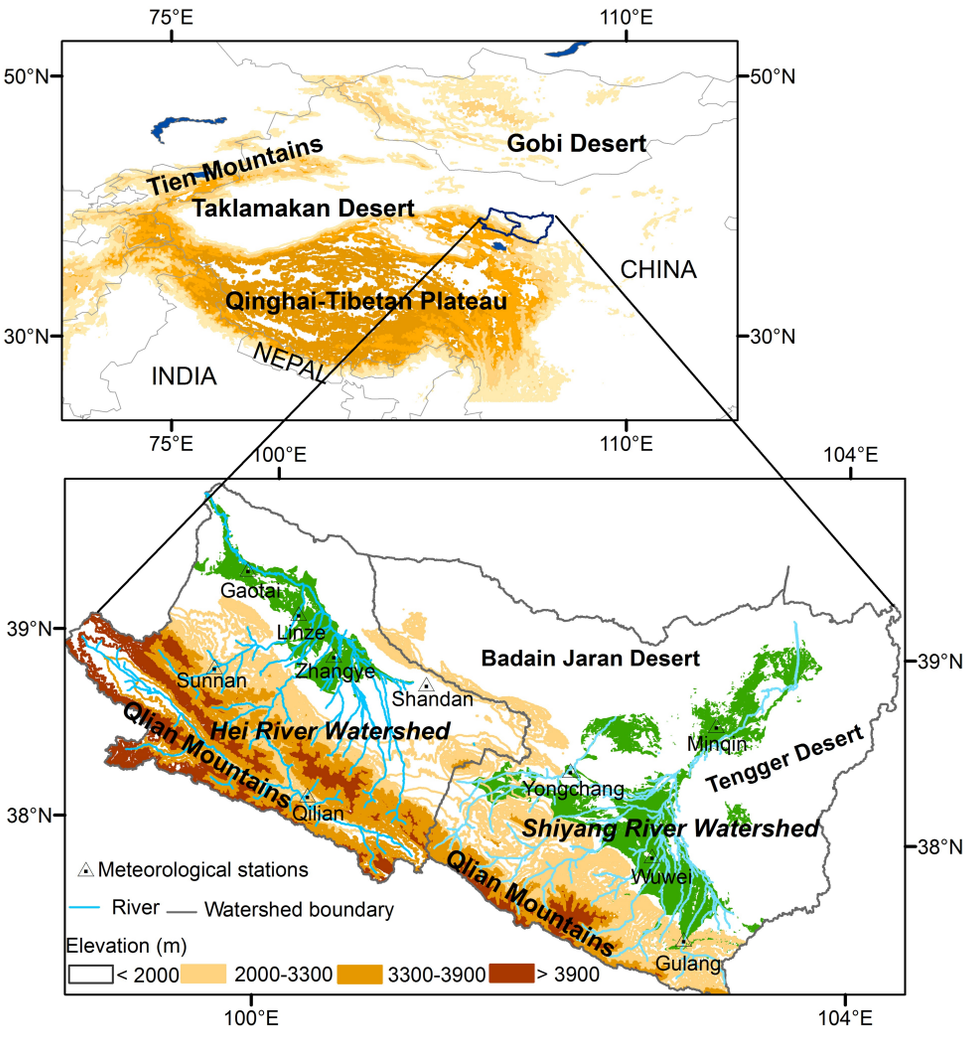

Figure 1. (a) Location of the study area along the northeast flank of the Qinghai-Tibetan Plateau. Yellow and orange areas correspond to mountain ranges and plateau, respectively. Map (b) gives the physical boundaries of the Shiyang and Hei River watersheds, respectively. Green areas in (b) illustrate the geographic extent of major oases at the base of the Qilian Mountains. Meteorological data relevant to the study were collected at individual climate stations identified in (b).

Presence of the Qinghai-Tibetan Plateau at the south of the study area blocks the northward passage of southwest monsoonal precipitation and the westerly airflow on the northern side of the plateau interferes with southerly airflow from reaching the region [83]. Dry northwesterly winds during summer generated from the Azores high pressure system and cold dry northerly winds during the winter generated from the Siberian high pressure system limit the outside contribution of moisture to this area [84]. Cyclic exchange of atmospheric

http://dx.doi.org/10.5772/52812

and surface and shallow subsurface water in the region forms a nearly perfect close system [74]. ET in the series of oases at the base of the Qilian Mountains is shown to play an important role in the recycling of water in the region and seasonal evolution of snow cover in the Qilian Mountains [7, 85].

5. Seasonal and annual variation of AET for different landcover types

5.1. Landcover classification

The MODIS annual global landcover map currently available (as of 2012) is produced from seven spectral maps, BRDF-adjusted reflectance, T_s, EVI, and an application of supervised classification using ground data from 1860 field sites [86]. Assessments of the product have shown that this map is not entirely realistic for zones of transition or for mountainous regions [87]. Improved landcover definition at regional or local scales with supervised classification usually involves much greater amounts of ground data that are normally available for most regions. Recently, decision tree-based classification has been applied to RS-data and has been shown to produce better results than other classification systems based on maximum likelihood or unsupervised clustering and labeling [88]. One advantage of decision tree-based classification is that it is able to use local knowledge of vegetation characteristics together with other pertinent data, such as terrain characteristics. In the current study, we use chronological-sequences of MODIS-based EVI and digital terrain information (e.g., aspect, elevation) to classify landcover with decision trees.

Vegetation distribution in the study area has a unique preferential association with elevation, slope, and slope direction [89]. North-facing slopes of the Qilian Mountains support alpine meadow at elevations between 2,500 to 3,300 m AMSL. At elevations above 3,300 m AMSL, deciduous shrubs represent the most dominant vegetation type. Isolated patches of conifer forests in the Qilian Mountains are classified as a separate ecoregion [90] found at elevations between 2,500 m to 3,300 m AMSL. Vegetation density and seasonal vegetation growth vary as a function of vegetation type and, consequently, landcover.

Based on vegetation site preferences, the study area is subdivided into four main elevation zones defined by elevations:

i. < 2,500;

ii. between 2,500 to 3,300;

iii. between 3,300 to 3,900; and

iv. > 3,900 m AMSL.

Different landcover types in these elevation zones were then identified based on EVI and terrain attributes, in particular slope orientation (aspect). Landcover types and their discrimination are summarized in Table 2.

Elevation zone	Landcover	Discrimination criteria
Zone 1 (< 2,500 m AMSL)	Desert	Mean growing-season EVI < 0.1130
	Crop	Maximum growing-season EVI > 0.27 and mean growing-season EVI < 0.1130
	Dense grass	Maximum growing-season EVI > 0.27, but different from cropland
	Sparse grass and/or shrub	Mean growing-season EVI between 0.113-0.27
Zone 2 (2,500-3,300 m AMSL)	Alpine meadow	Maximum growing-season EVI > 0.27 on north-facing slopes
	Coniferous forest	Maximum growing-season EVI > 0.27 on other than north-facing slopes
	Sparse grass and/or shrub	Mean growing-season EVI between 0.113 – 0.27
	Bare land	Mean growing-season EVI < 0.113
Zone 3 (3,300-3,900 m AMSL)	Deciduous shrub	Maximum growing-season EVI > 0.27
	Bare land	Mean growing-season EVI < 0.113
Zone 4 (> 3,900 m AMSL)	Sparse shrub	Mean growing-season EVI between 0.113-0.27
	Snow and/or ice	Mean growing-season EVI < 0.113

Table 2. Landcover definition as a function of elevation zone, EVI, and slope orientation (aspect).

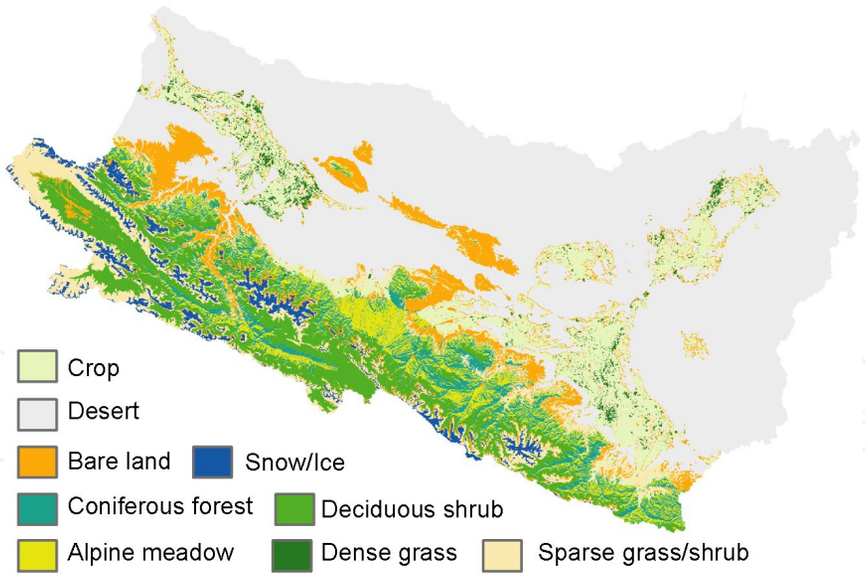

Figure 2. Study-area distribution of dominant landcover types.

Ten landcover maps were generated for 2000-2009 using the classification standards summarized in Table 2. From these maps, a final landcover composite ($LCOV_{dom}$ for all image pixels; Fig. 2) was then created based on a pixel-level, landcover-dominance evaluation, i.e.,

http://dx.doi.org/10.5772/52812

$$LCOV_{dom}\Big|_{for\ all\ pixels} = \underset{i=2000-2009}{Majority}(LCOV_i)\Big|_{for\ all\ pixels}, \quad (28)$$

where $LCOV_i$ and $LCOV_{dom}$ represent landcover at the pixel-level for individual years (2000-2009) and the dominant landcover over the same ten-year time period, respectively.

5.2. Study-area AET variation for different landcover types

Monthly AET for the study area was calculated using the complementary method of *Venturini et al.* [56] for the period of 2000-2009. Computed AET was compared with ET_o calculated from pan evaporation data (Fig. 3) corrected with season-specific coefficients reported in [91]. Pan evaporation coefficients were calculated by relating 50 years of pan evaporation data collected at 580 climate stations distributed across China to ET_o calculated for the same stations with the FAO Penman-Monteith equation. Pan evaporation coefficients by *Chen et al.* [91] varied from 0.45 to 0.54 from spring to winter. The scattergraphs in Fig. 3 show that modeled AET has very high positive correlation with ET_o for both watersheds ($R^2 > 0.78$; Fig. 3a for the Shiyang and Fig. 3b for the Hei River watershed). The line and error graphs in Fig. 3 are generated from AET-values extracted at the location of four meteorological stations within the Liangzhou, Minqin, and Zhangye oases (Fig. 1). The lines represent mean total monthly AET based on 2000-2009 data; error bars represent standard deviation of corresponding values. Modeled AET display seasonal patterns similar to those expressed in ET_o, but at substantially reduced levels (Fig. 3). This discrepancy can be rationalized by three important realities, i.e.,

i. modeled AET represents the average conditions of individual image pixels (covering 62,500 m^2) and not points;

ii. surface moisture and vegetation conditions and water-vapor-transfer resistances are openly different from those driving ET_o (i.e., open water vs. soil-plant environments); and

iii. pan evaporation coefficients are based on seasonal averages independent of location.

Spatially-distributed average total monthly AET was calculated by averaging monthly AET-images generated for the 2000-2009 period (Fig. 4). Yearly total growing-season AET was calculated by summing AET from April-October of each year (Fig. 5). From Fig. 4, it is clear that AET in the watershed is very low (≤ 25 mm $month^{-1}$) during winter (January-March and October-December periods) and progressively higher in summer (> 75 mm $month^{-1}$). AET reaches its maximum during the June-August period and begins to decrease prior the start of winter. Both monthly and total growing-season AET reveals greatest AET in the oases and low-to-mid-slope positions of the Qilian Mountains and lowest in the deserts (not shown) and high-elevation portions of the Qilian Mountains. Within-year variation in AET also appears within the same elevation bands due to changes in vegetation type. Comparison of chronological-series of monthly AET for three landcover types is shown in Fig. 6. For most years, forest landcover is shown to contribute the most to AET in the Shiyang River

watershed; crop cover, however, contributes the most in the Hei River watershed (Fig. 6). For the two watersheds, areas sparse of vegetation (as defined in Table 2) consistently contribute the least to AET during the growing seasons of 2000-2009.

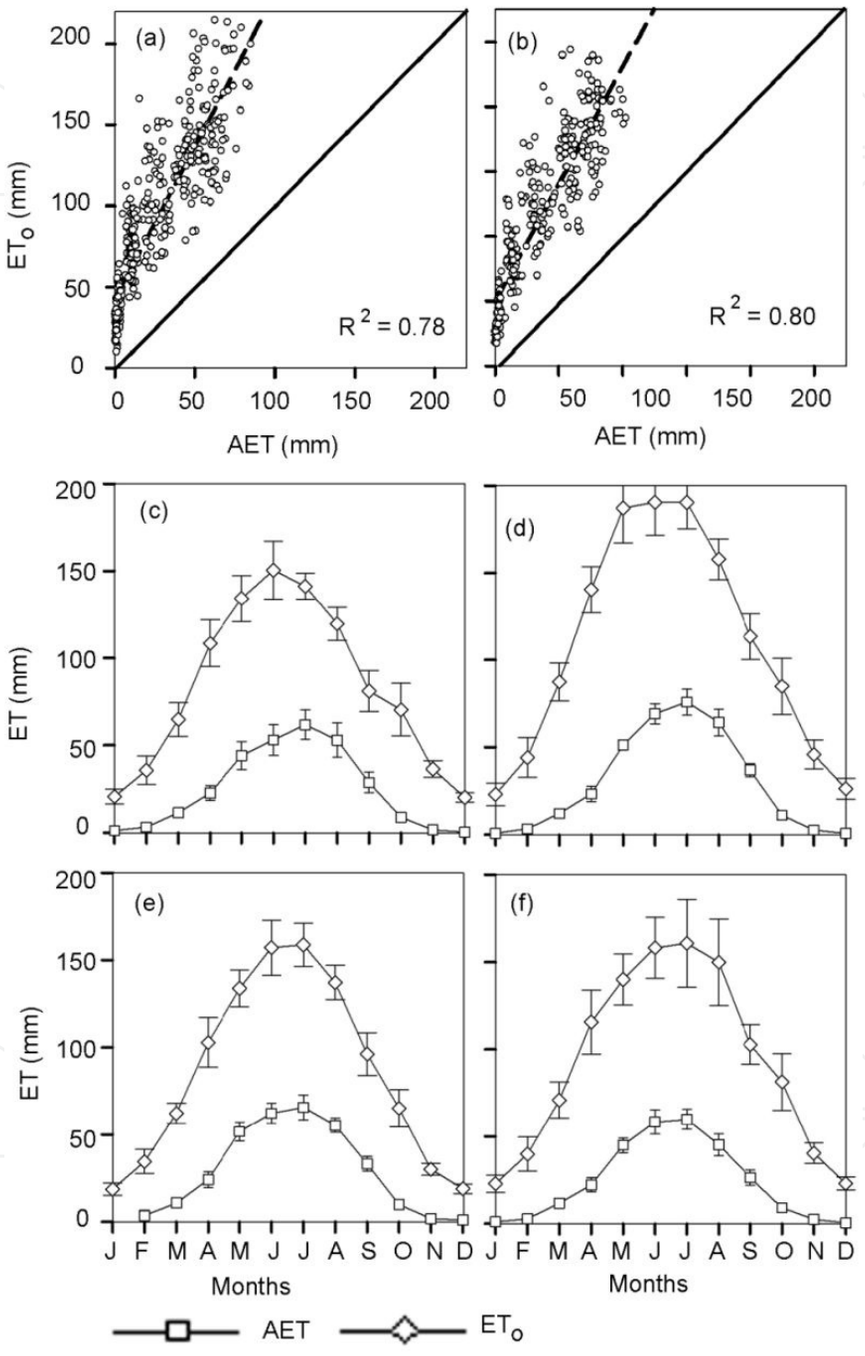

Figure 3. Comparison of monthly AET against ET_o calculated from pan evaporation data over a ten-year (2000-2009) period. Dashed lines in (a) and (b) are lines of regression fitted to the ET_o-to-AET data pairs; R^2 is the coefficient of determination. Line and error graphs of monthly AET and ET_o [i.e., (c)-(f)] are based on modeled AET-data extracted at the location of four climate stations, including Wuwei (c) and Minqin (d), representing the Shiyang River watershed, and Zhangye (e) and Shandan (f), representing the Hei River watershed and pan evaporation data.

http://dx.doi.org/10.5772/52812

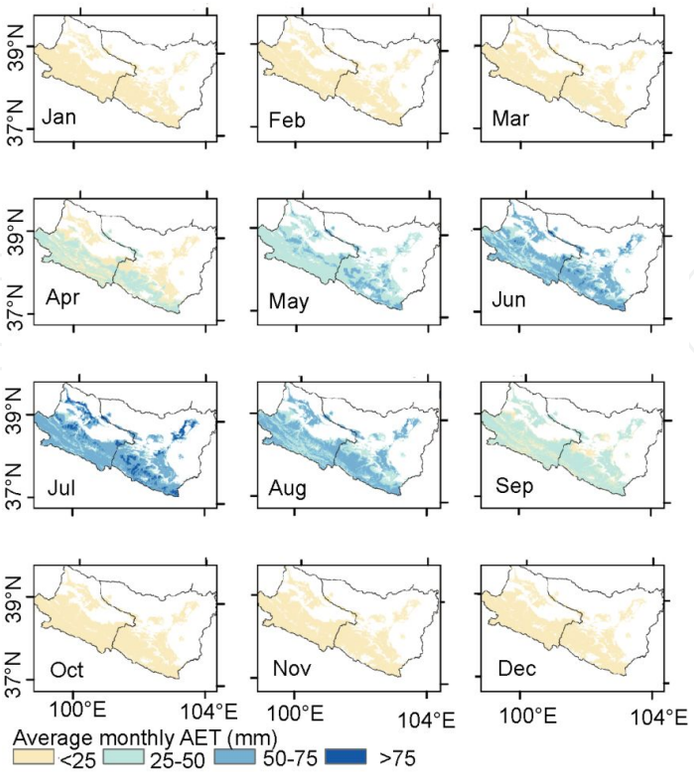

Figure 4. Study-area distribution of monthly AET averaged over the 2000-2009 period.

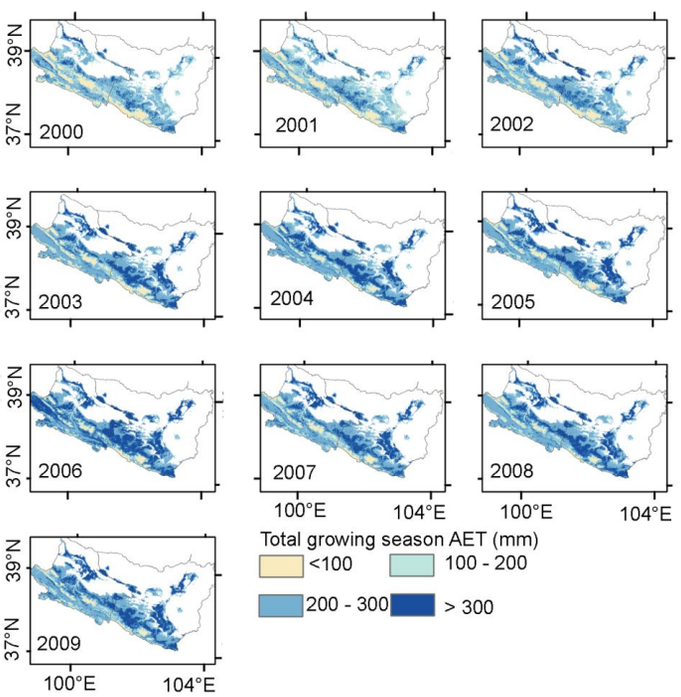

Figure 5. Study-area distribution of total growing-season (April-October period) AET for the 2000-2009 period.

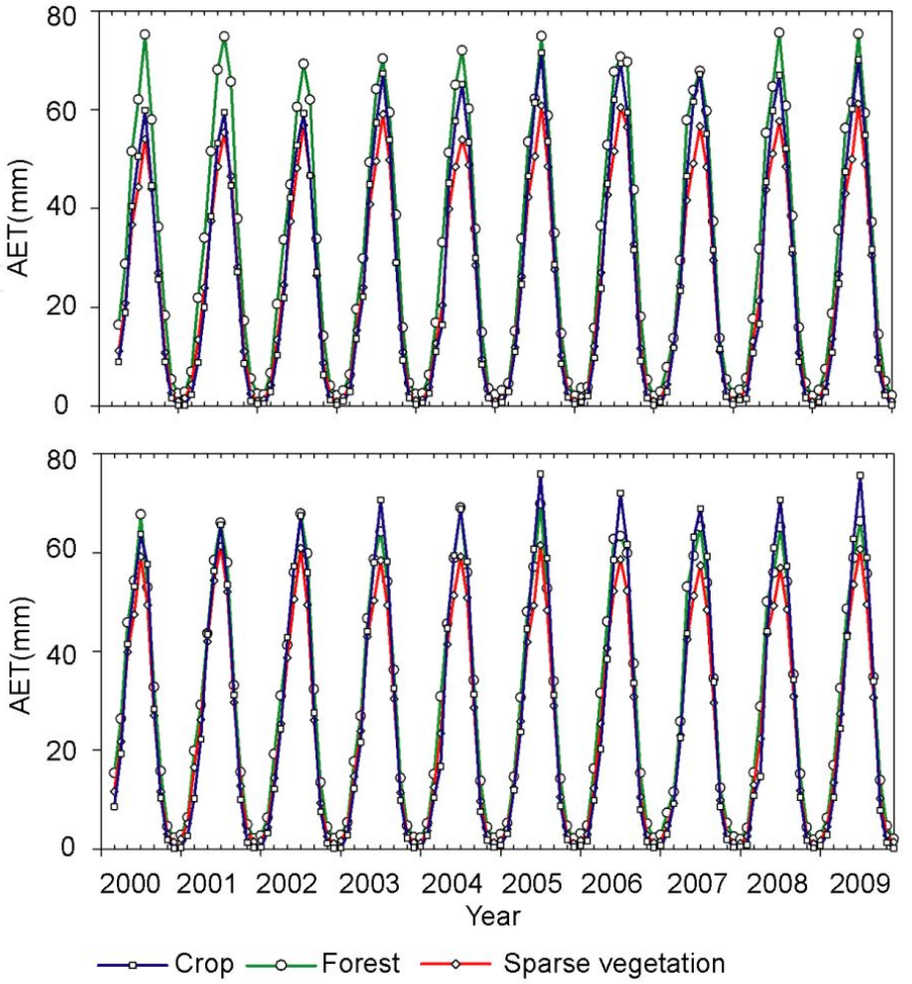

Figure 6. Monthly average AET (mm) for three landcover types; the upper graph gives monthly AET for the Shiyang River watershed, whereas the bottom graph gives it for the Hei River watershed.

5.3. Vegetation influence on AET

Using EVI as an indicator of vegetation density and vitality, monthly AET was compared with same-month EVI extracted at 220 randomly distributed points across the study area for different landcover types. Scattergraphs using all points and partitioned according to landcover type (Fig. 7) show that independent-evaluations of AET have an overall positive correlation with same-month EVI; the strength of correlation (R^2), however, varies with landcover type. Strongest correlation occurs for cropland areas and weakest, for areas sparse of vegetation.

http://dx.doi.org/10.5772/52812

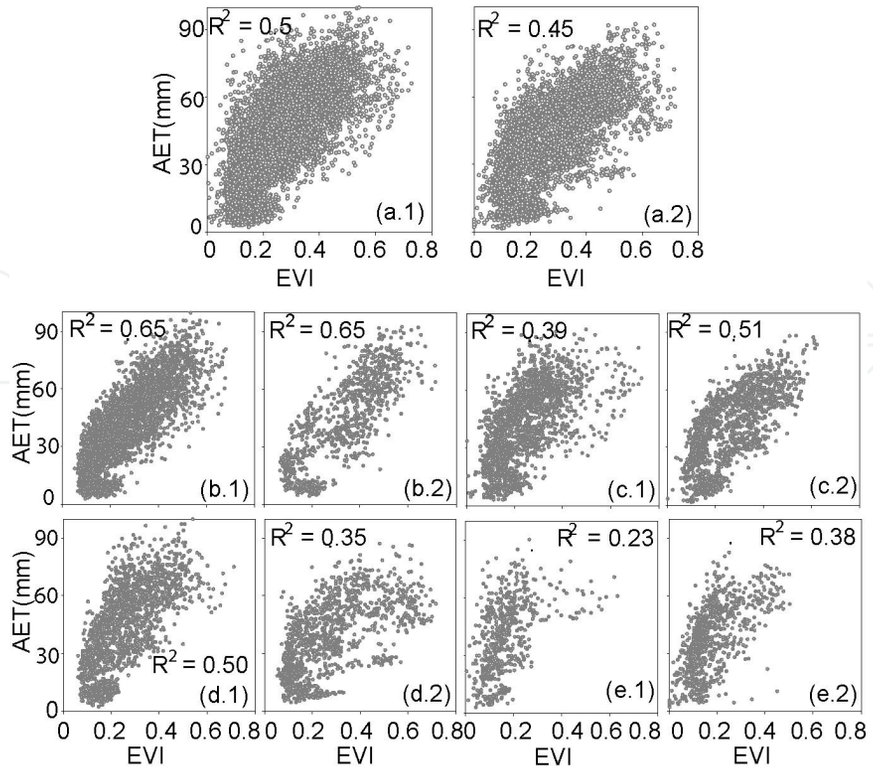

Figure 7. Scattergraphs showing AET as a function of same-month EVI for different vegetation covertypes for the two watersheds (labels with 1 refer to the Shiyang River watershed and 2, to the Hei River watershed): a.1 and a.2 represents all landcover types combined; b.1 and b.2 for crop cover; c.1 and c.2 for forest cover; d.1 and d.2 for dense grass cover; and e.1 and e.2 for sparse grass or shrub cover.

6. Conclusions

This chapter provides

i. a summary of methodologies available to estimate AET at point to regional scales, and

ii. case-study calculations of AET for two watersheds in NW China based on the complementary relationship of *Venturini et al.* [56].

The complementary relationship of *Venturini et al.* is considered appropriate for complex landscapes of NW China, because of the method's independence from wind velocity, its overall accurracy, and its ability to regionalize AET-calculations with assistance of RS-data as input. Because of the frequent acquisition of MODIS data (primary input datatype to the calculation of AET), AET-calculations can be updated frequently. For NW China, AET-calculations at 250-m resolution were carried out on a monthly interval over a ten-year time period (2000-2009). Based on a landcover map generated from decision-tree classification and landcover-dominance analysis, regional AET was partitioned along three vegetation-dominated landcover types. Forest and crop landcover types were shown to contribute the most

to AET across the study area, particularly in lowland areas. Areas of sparse vegetation (among the three landcover types) contributed the least to regional AET. This supports the view that the state and abundance of vegetation (defined here by EVI), particularly in the lowlands and low-to-mid-slope positions of the Qilian Mountains, have an important influence on regional AET and on the water budget of the study area.

Author details

Mir A. Matin and Charles P.-A. Bourque*

*Address all correspondence to: cbourque@unb.ca

Faculty of Forestry and Environmental Management, University of New Brunswick, Canada

References

[1] Allen, R. G., Pereira, L. S., Raes, D., & Smith, M. (1998). Crop evapotranspiration-Guidelines for computing crop water requirements. *Rome: FAO- Food and Agriculture Organization of the United Nations.*

[2] Thornthwaite, C. W. (1948). An Approach toward a Rational Classification of Climate. *Geographical Review*, 38(1), 55-94.

[3] Curry, L. (1963). Thornthwaites Potential Evapotranspiration Term. *Annals of the Association of American Geographers*, 53(4), 585.

[4] Luo, X., Wang, K., Jiang, H., Sun, J., Xu, J., Zhu, Q., et al. (2010). Advances in research of land surface evapotranspiration at home and abroad. *Sciences in Cold and Arid Regions*, 2(2), 104-11.

[5] Mu, Q., Heinsch, F. A., Zhao, M., & Running, S. W. (2007). Development of a global evapotranspiration algorithm based on MODIS and global meteorology data. Remote sensing of environmentDec 28; , 111(4), 519-36.

[6] Verstraeten, W. W., Veroustraete, F., & Feyen, J. (2008). Assessment of evapotranspiration and soil moisture content across different scales of observation. Sensors. Jan; , 8(1), 70-117.

[7] Bourque, C. P.-A, & Hassan, Q. K. (2009). Vegetation control in the long-term self-stabilization of the Liangzhou Oasis of the Upper Shiyang river watershed of West-Central Gansu, Northwest China. *Earth Interactions*, 13, 1-22.

[8] Helldén, U. (2008). A coupled human-environment model for desertification simulation and impact studies. *Global and Planetary Change*, 64(3-4), 158-168.

[9] Pielke, R. A., & Avissar, R. (1990). Influence of landscape structure on local and regional climate. *Landscape Ecology*, 4(2), 133-55.

[10] Bonan, G. B. (2008). Ecological Climatology, Concepts and Applications. *2nd edition ed. New York: Cambridge University Press*.

[11] Greene, E. M., Liston, G. E., & Pielke, R. A. (1999). Relationships between landscape, snowcover depletion, and regional weather and climate. Hydrological processes. Oct; , 13(14-15), 2453-66.

[12] Pielke, R. A., Adegoke, J., Beltran-Przekurat, A., Hiemstra, C. A., Lin, J., Nair, U. S., et al. (2007). An overview of regional land-use and land-cover impacts on rainfall. Tellus Series B-Chemical and Physical Meteorology. Jul; , 59(3), 587-601.

[13] Pielke, R. A. (2001). Influence of the spatial distribution of vegetation and soils on the prediction of cumulus convective rainfall. *Review of Geophysics*, 39(2), 151-77.

[14] Raddatz, R. L. (2007). Evidence for the influence of agriculture on weather and climate through the transformation and management of vegetation: Illustrated by examples from the Canadian Prairies. *Agricultural and Forest Meteorology*, 142(2-4), 186-202.

[15] Rose, C. W., & Sharma, M. L. (1984). Summary and Recommendations of the Workshop on Evapotranspiration from Plant-Communities. *Agricultural Water Management*, 8(1-3), 325-42.

[16] Bowen, I. S. (1926). The ratio of heat losses by conduction and by evaporation from any water surface. Physical Review. Jun; , 27(6), 779-87.

[17] Baldocchi, D. D. (2003). Assessing the eddy covariance technique for evaluating carbon dioxide exchange rates of ecosystems: past, present and future. *Global Change Biology*, 9, 1-14.

[18] Rana, G., & Katerji, N. (2000). Measurement and estimation of actual evapotranspiration in the field under Mediterranean climate: a review. European Journal of Agronomy Aug; , 13(2-3), 125-153.

[19] Holmes, J. W. (1984). Measuring Evapotranspiration by Hydrological Methods. *Agricultural Water Management*, 8(1-3), 29-40.

[20] Wright, J. L. (1991). Using Weighing Lysimeters to Develop Evapotranspiration Crop Coefficients. *Lysimeters for Evapotranspiration and Environmental Measurements*, 191-9.

[21] Pieri, P., & Fuchs, M. (1990). Comparison of Bowen-Ratio and Aerodynamic Estimates of Evapotranspiration. Agricultural and Forest MeteorologyFeb; , 49(3), 243-56.

[22] Verma, S. B. (1987). Aerodynamic resistance to transfer of heat, mass and momentum. Estimation of aerial evapotranspiration. *Vancouver, B.C., Canada: International association of hydrological sciences.*

[23] Liu, S. M., Sun, Z. P., Wang, H. M., Li, X. W., & Han, L. J. (2003). An intercomparison study on models of estimating- The aerodynamic resistance. *Igarss: Ieee International Geoscience and Remote Sensing Symposium, Vols I- Vii, Proceedings*, 3341-3.

[24] Drexler, J. Z., Snyder, R. L., Spano, D., & Paw, K. T. U. (2004). A review of models and micrometeorological methods used to estimate wetland evapotranspiration. Hydrological processes. Aug 15; , 18(11), 2071-101.

[25] Denmead, O. T. (1984). Plant Physiological Methods for Studying Evapotranspiration- Problems of Telling the Forest from the Trees. *Agricultural Water Management*, 8(1-3), 167-89.

[26] Glenn, E. P., Huete, A. R., Nagler, P. L., Hirschboeck, K. K., & Brown, P. (2007). Integrating remote sensing and ground methods to estimate evapotranspiration. *Critical Reviews in Plant Sciences*, 26(3), 139-68.

[27] Bastiaanssen, W. G. M., Menenti, M., Feddes, R. A., & Holtslag, A. A. M. (1998). A remote sensing surface energy balance algorithm for land (SEBAL)- 1. Formulation. Journal of Hydrology Dec; , 213(1-4), 198-212.

[28] Kustas, W. P., & Norman, J. M. (1999). Evaluation of soil and vegetation heat flux predictions using a simple two-source model with radiometric temperatures for partial canopy cover. Agricultural and Forest Meteorology. Apr 1; , 94(1), 13-29.

[29] Su, Z. (2002). The surface energy balance system (SEBS) for estimation of turbulent heat fluxes. *Hydrology and Earth System Sciences*, Feb, 6(1), 85-99.

[30] Penman, H. L. (1948). Natural evaporation from open water, bare soil and grass. *Proceedings of the Royal Society of London Series A, Mathematical and Physical Sciences*, 193(1032), 120-45.

[31] Penman, H. L. (1956). Evaporation: an introductory survey. *Netherland Journal of Agricultural Science*, 4, 9-29.

[32] Priestley, C. H. B., & Taylor, R. J. (1972). On the assessment of surface heat flux and evaporation using large-scale parameters. *Monthly Weather Review*, 100(2).

[33] Bouchet, R. J. (1963). Evapotranspiration re ´elle et potentielle, signification climatique. *International Association of Hydrological Sciences, Proceedings of General Assmbly; Berkely, California: California Symposium Publication.*

[34] Granger, R. J. (1989). A complementary relationship approach for evaporation from nonsaturated surfaces. *Journal of Hydrology.*, Nov, 111(1-4), 31-8.

[35] Archer, M. D., & Barber, J. (2004). Molecular to Global Photosynthesis. *London: Imperial College Press*.

[36] Bourque-A, C. P., & Gullison, J. J. (1998). A technique to predict hourly potential solar radiation and temperature for a mostly unmonitored area in the Cape Breton Highlands. *Canadian Journal of Soil Science*, 78, 409-20.

[37] Bourque-A, C. P., Meng-R, F., Gullison, J. J., & Bridgland, J. (2000). Biophysical and potential vegetation growth surfaces for a small watershed in northern Cape Breton Island, Nova Scotia, Canada. *Canadian Journal of Forest Research*, 30(8), 1179-95.

[38] Dubayah, R., & Rich, P. M. (1995). Topographic solar-radiation models for GIS. International Journal of Geographical Information SystemsJul-Aug; , 9(4), 405-19.

[39] Fu, P., & Rich, P. M. (2000). The Solar Analyst 1.0 Manual.

[40] Li, Z. L., Tang, R. L., Wan, Z. M., Bi, Y. Y., Zhou, C. H., Tang, B. H., et al. (2009). A Review of Current Methodologies for Regional Evapotranspiration Estimation from Remotely Sensed Data. Sensors. May; , 9(5), 3801-53.

[41] Brutsaert, W. (1999). Aspects of bulk atmospheric boundary layer similarity under free-convective conditions. Reviews of GeophysicsNov; , 37(4), 439-51.

[42] Meneti, M. (1984). Physical Aspects and Determination of Evaporation in Deserts Applying Remote-Sensing Techniques- Menenti,M. *Ground Water*, 22(6), 801-2.

[43] Monteith, J. L. (1965). Evaporation and environment. *Symposia of the Society for Experimental Biology*, 19, 205-34.

[44] Cleugh, H. A., Leuning, R., Mu, Q. Z., & Running, S. W. (2007). Regional evaporation estimates from flux tower and MODIS satellite data. Remote Sensing of EnvironmentFeb 15; , 106(3), 285-304.

[45] Huete, A. R., Didan, K., Miura, T., rodriguez, E. P., Gao, X., & Fereira, L. G. (2002). Overview of the radiometric and biophysical performance of the MODIS vegetation indices. *Remote sensing of environment*, 83(1-2), 195-213.

[46] Mu, Q., Zhao, M. S., & Running, S. W. (2011). Improvements to a MODIS global terrestrial evapotranspiration algorithm. Remote sensing of environmentAug 15; , 115(8), 1781-800.

[47] Morton, F. I. (1969). Potential evaporation as a manifestation of regional evaporation. *Water Resources Research*, 5(6), 1244-55.

[48] Szilagyi, J., Hobbins, M. T., & Jozsa, J. (2009). Modified advection-aridity model of evapotranspiration. Journal of Hydrologic EngineeringJun; , 14(6), 569-74.

[49] Szilagyi, J. (2001). On Bouchet's complementary hypothesis. Journal of HydrologyJun 1 , 246(1-4), 155-8.

[50] Granger, R. J., & Gray, D. M. (1989). Evaporation from natural nonsaturated surfaces. Journal of Hydrology. Nov; , 111(1-4), 21-9.

[51] Brutsaert, W., & Stricker, H. (1979). An advection-aridity approach to estimate actual regional evapotranspiration. *Water Resources Research*, 15(2), 443-50.

[52] Morton, F. I. (1983). Operational estimates of aerial evaporation and their siginificance to science and practice of hydrology. *Journal of hydrology*, 66, 1-76.

[53] Hobbins, M. T., Ramirez, J. A., Brown, T. C., & Claessens, L. H. J. M. (2001). The complementary relationship in estimation of regional evapotranspiration: The Complementary Relationship Areal Evapotranspiration and Advection-Aridity models. Water Resources Research. May; , 37(5), 1367-87.

[54] Ramirez, J. A., Hobbins, M. T., & Brown, T. C. (2005). Observational evidence of the complementary relationship in regional evaporation lends strong support for Bouchet's hypothesis. *GEOPHYSICAL RESEARCH LETTERS.*, Aug 5;, 32(15).

[55] Xu, C. Y., & Singh, V. P. (2005). Evaluation of three complementary relationship evapotranspiration models by water balance approach to estimate actual regional evapotranspiration in different climatic regions. Journal of Hydrology. Jul 12; , 308(1-4), 105-21.

[56] Venturini, V., Islam, S., & Rodrigue, Z. L. (2008). Estimation of evaporative fraction and evapotranspiration from MODIS products using a complementary based model. Remote Sensing of EnvironmentJan 15; , 112(1), 132-41.

[57] Kalma, J. D., Mc Vicar, T. R., & Mc Cabe, M. F. (2008). Estimating Land Surface Evaporation: A Review of Methods Using Remotely Sensed Surface Temperature Data. Surveys in Geophysics. Oct; , 29(4-5), 421-69.

[58] Justice, C. O., Vermote, E., Townshend, J. R. G., Defries, R., Roy, D. P., Hall, D. K., et al. (1998). The Moderate Resolution Imaging Spectroradiometer (MODIS): Land remote sensing for global change research. IEEE TRANSACTIONS ON GEOSCIENCE AND REMOTE SENSING. Jul; , 36(4), 1228-49.

[59] Ramachandra, B., Justice, C. O., & Abrams, MJ. (2011). Land remote sensing and global environmental change: NASA's earth obeserving system and science of ASTER and MODIS. *New York: Springer*.

[60] Bisht, G., Venturini, V., Islam, S., & Jiang, L. (2005). Estimation of the net radiation using MODIS (Moderate Resolution Imaging Spectroradiometer) data for clear sky days. *Remote sensing of environment.*, Jul 15;, 97(1), 52-67.

[61] Wan, Z., Zhang, Y., Zhang, Q., & Li, Z. L. (2004). Quality assessment and validation of the MODIS global land surface temperature. International Journal of Remote SensingJan; , 25(1), 261-74.

[62] Wan, Z. M., & Dozier, J. (1996). A generalized split-window algorithm for retrieving land-surface temperature from space. IEEE TRANSACTIONS ON GEOSCIENCE AND REMOTE SENSING. Jul; , 34(4), 892-905.

[63] Petitcolin, F., & Vermote, E. (2002). Land surface reflectance, emissivity and temperature from MODIS middle and thermal infrared data. *Remote sensing of environment*, Nov;, 83(1-2), 112-34.

[64] Huete, A. R., Litu, H. Q., Batchily, K., & Leeuwen, Wv. (1997). A comparison of vegetation indices over a global set of TM images for EOS-MODIS. *Remote Sensing of Environment*, 59(3), 440-51.

[65] Wardlow, B. D., & Egbert, S. L. (2010). A comparison of MODIS 250-m EVI and NDVI data for crop mapping: a case study for southwest Kansas. *International Journal of Remote Sensing*, 31(3), 805-30.

[66] Davidson, A., & Wang, S. S. (2005). Spatiotemporal variations in land surface albedo across Canada from MODIS observations. Canadian Journal of Remote SensingOct; , 31(5), 377-90.

[67] Strahler, A. H., & Muller-P, J. (1999). NASA MODIS BRDF/Albedo product: algorithm and theoritical basis document, version 5.0.

[68] Schaaf, C. B., Gao, F., Strahler, A. H., Lucht, W., Li, X. W., Tsang, T., et al. (2002). First operational BRDF, albedo nadir reflectance products from MODIS. Remote sensing of environment. Nov; , 83(1-2), 135-48.

[69] Jimenez-Munoz, J. C., Sobrino, J. A., Mattar, C., & Franch, B. (2010). Atmospheric correction of optical imagery from MODIS and Reanalysis atmospheric products. Remote Sensing of Environment. Oct 15; , 114(10), 2195-210.

[70] Seeman, S. W., Borbas, E. E., Li, J., Menzel, W. P., & Gumley, L. E. (2012). Modis atmospheric profile retrieval, algorithm theoritical basis document version 6 reference number ATBD-MOD07. http://modis.gsfc.nasa.gov/data/atbd/atbd_mod07.pdf, accesses on June 20,)., *Madison, WI: Cooperative Institute for Meteorological Satellite Studies2006*.

[71] Li, X. Y., Xiao, D. N., He, X. Y., Chen, W., & Song, D. M. (2007). Factors associated with farmland area changes in arid regions: a case study of the Shiyang river basin, Northwestern China. *Frontiers in Ecology and the Environment*, Apr;, 5(3), 139-44.

[72] Gu, J., Li, X., & Huang, C. L. (2008). Land cover classification in Heihe river basin with time series MODIS NDVI data. Fifth International Conference on Fuzzy Systems and Knowledge Discovery Proceedings , 2, 477-81.

[73] Ma, M. G., & Frank, V. (2006). Interannual variability of vegetation cover in the Chinese Heihe river basin and its relation to meteorological parameters. *International Journal of Remote Sensing*, Aug 20;, 27(16), 3473-86.

[74] Ji, X. B., Kang, E. S., Chen, R. S., Zhao, W. Z., Zhang, Z. H., & Jin, B. W. (2006). The impact of the development of water resources on environment in arid inland river basins of Hexi region, Northwestern China. Environmental Geology. Aug; , 50(6), 793-801.

[75] Olson, D. M., Dinerstein, E., Wikramanayake, E. D., Burgess, N. D., Powell, G. V. N., Underwood, E. C., et al. (2001). Terrestrial ecoregions of the world: A new map of life on earth. *BioScience*, 51(11), 933-8.

[76] Zhao, C., Nan, Z., & Cheng, G. (2005). Methods for estimating irrigation needs of spring wheat in the middle Heihe basin, China. *Agricultural Water Management*, 75(1), 54-70.

[77] Carpenter, C. (2001a). Alashan Plateau semi-desert (PA1302). *World Wildlife Fund ©*, [accessed on 2011 13 December]; Available from:, https://secure.worldwildlife.org/wildworld/profiles/terrestrial/pa/pa1302_full.html.

[78] Wang, J. S., Feng, J. Y., Yang, L. F., Guo, J. Y., & Pu, Z. X. (2009). Runoff-denoted drought index and its relationship to the yields of spring wheat in the arid area of Hexi corridor, Northwest China. Agricultural Water Management. Apr; , 96(4), 666-76.

[79] Jin, X. M., Schaepman, M., Clevers, J., Su, Z. B., & Hu, G. C. (2010). Correlation between annual runoff in the Heihe river to the vegetation cover in the Ejina Oasis (China). *Arid Land Research and Management*, 24(1), 31-41.

[80] Roe, G. H. (2005). Orographic precipitation. *Annual Review of Earth and Planetary Sciences*, 33, 645-71.

[81] Zhu, Y. H., Wu, Y. Q., & Drake, S. (2004). A survey: obstacles and strategies for the development of ground-water resources in arid inland river basins of Western China. Journal of Arid EnvironmentsOct; , 59(2), 351-67.

[82] Kang, S., Su, X., Tong, L., Shi, P., Yang, X., Abe, Y., et al. (2009). The impacts of human activities on the water-land environment of the Shiyang River Basin, an arid region in Northwest China. *Hydrological Sciences Journal*, 49(3), 413-27.

[83] Liu, S., Zhang, C., Zhao, J., Wang, S., & Huang, Y. (2005). Study on the changes of water vapor over Hexi corridor and adjacent regions. *Acta Meteorologica Sinica*, 20, 108-21.

[84] Warner, T. T. (2004). Desert Meteorology. *London: Cambridge University Press*.

[85] Bourque, C. P. A., & Mir, M. A. (2012). Seasonal snow cover in the Qilian Mountains of Northwest China: Its dependence on oasis seasonal evolution and lowland production of water vapour. *Journal of Hydrology*, 454-455, 141-51.

[86] Friedl, M. A., Sulla-Menashe, D., Tan, B., Schneider, A., Ramankutty, N., Sibley, A., et al. (2010). MODIS Collection 5 global land cover: Algorithm refinements and characterization of new datasets. *Remote sensing of environment.*, Jan 15;, 114(1), 168-82.

[87] Liang, L., & Gong, P. (2010). An Assessment of MODIS Collection 5 Global Land Cover Product for Biological Conservation Studies. *18th International Conference on Geoinformatics.*

[88] Friedl, M. A., & Brodley, C. E. (1997). Decision tree classification of land cover from remotely sensed data. Remote sensing of environment. Sep; , 61(3), 399-409.

[89] Jin, X. M., Zhang-K, Y., Schaepman, M. E., Clevers, J. G. P. W., & Su, Z. (2008). Impact of elevation and aspect on the spatial distribution of vegetation in the qilian mountain area with remote sensing data. *The International Archives of the Photogrammetry, Remote Sensing and Spatial Information Sciences*, 37, Part B7).

[90] Carpenter, C. (2001b). Montane Grasslands and Shrublands. *World Wildlife Fund ©*, [accessed on 2011 13 Dec]; Available from:, http://www.worldwildlife.org/science/wildfinder/profiles/pa1015.html.

[91] Chen, D., Gao, G., Xu-Y, C., Guo, J., & Ren, G. (2005). Comparison of the Thornthwaite method and pan data with the standard Penman-Monteith estimates of reference evapotranspiration in China. *Climate Research*, 28, 123-32.

IntechOpen

IntechOpen